RSC Advances

PAPER

View Article Online
View Journal | View Issue

Cite this: *RSC Adv.*, 2018, **8**, 19289

Effect of cobalt addition on the corrosion behavior of near equiatomic NiTi shape memory alloy in normal saline solution: electrochemical and XPS studies†

Nawal D. Alqarni,[a] Joanna Wysocka,[b] Nader El-Bagoury,[ac] Jacek Ryl,[b] Mohammed A. Amin*[ad] and Rabah Boukherroub[e]

The electrochemical and corrosion (uniform and localized) behavior of a binary $Ni_{52}Ti_{48}$ shape memory alloy (SMA) and two ternary $Ni_{52}Ti_{48-x}Co_x$ (x = 1.5 and 4.0 wt%) SMAs were studied. Measurements were conducted in 0.9% NaCl solution at 37 °C employing various electrochemical methods. These include: linear polarization resistance (LPR), linear sweep voltammetry (LSV), chronoamperometry and dynamic electrochemical impedance spectroscopy (DEIS). Such measurements were complemented with scanning electron microscopy (SEM) and X-ray photoelectron spectroscopy (XPS) analysis. Results revealed that the addition of alloyed Co to NiTi significantly reduced the uniform corrosion rate of the studied SMA and greatly enhanced its pitting corrosion resistance. XPS measurements evidenced high stability of the passive layer and limited adsorption of chloride ions. Additionally, it was found that the passive layer remained primarily composed of titanium oxides. Microstructure changes accompanying the addition of Co were also used to account for its role in improving the corrosion resistance of these materials.

Received 7th March 2018
Accepted 17th May 2018

DOI: 10.1039/c8ra02031k

rsc.li/rsc-advances

1. Introduction

Shape Memory Alloys (SMAs) represent a unique class of materials exhibiting peculiar properties like the shape memory effect, the superelasticity associated with damping capabilities, high corrosion and extraordinary fatigue resistance.[1–5] Due to their potential use in an expanding variety of technological applications,[6–9] an increasing interest in the study of the SMAs has been witnessed in the research community during the previous decades.

SMAs are a distinguished category of shape memory materials with the ability to recover their shape when the temperature is increased even under high applied loads, resulting in high actuation energy densities. In addition, under specific conditions, SMAs can absorb and dissipate mechanical energy by undergoing a reversible hysteretic shape change when subjected to mechanical cyclic loading.[10–14] These unique characteristics of SMAs have made them popular for sensing and actuation, impact absorption and vibration damping applications. SMAs do, however, exhibit low frequency response. Higher actuation frequencies are achievable for a class of SMAs called magnetic shape memory alloys, which have recently been investigated. The application of SMAs spans a wide variety of industrial sectors such as aerospace, automotive, biomedical, and oil exploration. Over the past few decades, several key works have explored the microstructural mechanisms, engineering effects, and applications of shape memory alloys.[4,15,16]

Two important sets of characteristics, namely biofunctionality and biocompatibility control the performance of any biomedical material.[17,18] The former characteristic refers to the material ability to implement the required function, whereas the later determines material's compatibility with the body. For metallic biomaterials that are typically used in orthopedic implants, the functional requirements are high mechanical properties. These include yield strength, ductility, fatigue strength, and fracture toughness. The susceptibility of the material to corrosion and the effect the corrosion has on the tissue are the central aspects of biocompatibility.[17,18]

Shape memory alloys (SMAs), particularly NiTi SMA, have provided new insights into biomedical area for cardiovascular,

[a]*Materials Science and Engineering Group, Department of Chemistry, Faculty of Science, Taif University, 888 Hawiya, Saudi Arabia. E-mail: maaismail@yahoo.com*
[b]*Department of Electrochemistry, Corrosion and Materials Engineering, Chemical Faculty, Gdansk University of Technology, Narutowicza 11/12, 80-233 Gdansk, Poland*
[c]*Central Metallurgical Research and Development Institute (CMRDI), P. O. Box: 87 Helwan, Cairo, Egypt*
[d]*Department of Chemistry, Faculty of Science, Ain Shams University, 11566 Abbassia, Cairo, Egypt*
[e]*Univ. Lille, CNRS, Centrale Lille, ISEN, Univ. Valenciennes, UMR 8520 – IEMN, F-59000 Lille, France*

† Electronic supplementary information (ESI) available. See DOI: 10.1039/c8ra02031k

orthopedic and dental applications, and for making advanced surgical instruments, as they meet the requirements for orthopedic implantation, namely high biofunctionality and superior biocompatibility. Therefore, it is worth to highlight the orthopedic applications of this material.[19,20] In this regard, literature revealed numerous articles dealing with corrosion behavior of NiTi SMAs in various physiological environments.[21–23] For instance, Khalil-Allafi *et al.*[24] investigated the corrosion behavior of $Ni_{50.7}Ti_{49.3}$ SMA in two physiological environments, namely Ringer and NaCl (0.9%) solutions. Their topographical investigations demonstrated that the corrosion products are nearly same in the two solutions, even though the breakdown potential of the tested SMA in NaCl 0.9% solution was nobler than that measured in Ringer solution, revealing higher corrosion resistance, and hence lower toxicity, in the former solution.

Figueira *et al.*[25] studied the corrosion behavior of NiTi alloy (Ni 50.2 at%–Ti) in Hanks' solution at 37 °C, employing various electrochemical methods. They also considered other orthopedic implants, namely Ti–6Al–4V alloy and 316L stainless steel for comparison. It was found that the corrosion behavior of NiTi was almost similar to Ti than to Ni, as the chemical composition and protective characteristics of the passive oxide film formed on NiTi was similar to that formed on Ti. Based on these findings, the tested materials were ranked according to their corrosion resistance as: 316L stainless steel < NiTi < Ti–6Al–4V.[25]

Application of NiTi alloys in medical device is a result of their high corrosion resistance and biocompatibility in combination with increased modulus and high stiffness, as already highlighted.[26] Furthermore, Fasching *et al.*[27] investigated NiTi alloys containing 1–2% of cobalt and revealed that in comparison to NiTi alloys, NiTiCo has approximately 30% higher modulus, loading plateau and unloading plateau with similar biocompatibility and no reactivity in both investigated tests, namely: cytotoxicity and hemolysis. The yield strength improvement was also confirmed for NiTi alloys containing 2–10% Co addition.[28] To some extent, these results can be explained with two-step transformation, since martensitic transformation temperature is induced by Co addition separating it from R phase transformation. Alloys containing up to 10% of cobalt were also studied for material removal rate, microstructure and hardness with wire electro discharge machining technique.[29]

In order for these alloys to be successfully used, the effect of cobalt on the corrosion resistance properties must be well defined. Huang *et al.*[26] investigated the corrosion properties of these alloys in PBS solution, claiming similar behavior to cobalt-less NiTi alloys and no effect of galvanic corrosion within stent. These studies however were carried out in mild environment, where pitting or crevice corrosion is not to be expected.

Since Co-based alloys are generally much more resistant to localized corrosion effects, it is expected that sufficient Co additive into the alloy structure will increase its resistance to this form of damage, unless fretting or other mechanical damage occurs to the surface oxide.[30] Recently, we have investigated the electrochemical and corrosion behavior of Co-based magnetic shape memory alloys (MSMAs) in 0.5 M NaCl to reveal significant corrosion resistance of the studied MSMAs, evidenced through electrochemical and XPS studies, together with SEM/EDX examinations.[31]

However, the number of papers published so far is insufficient to adequately cover the bio-corrosion behavior of NiTi SMAs, particularly ternary NiTi-based SMAs,[32,33] and is not commensurate with the medical importance of these materials. In addition, literature revealed limited number of articles concerning the effect of Co addition on the corrosion behavior of NiTi SMAs.[31,34] Thus, the objective of this work was to investigate the passivation influence of alloyed Co during the uniform and pitting corrosion processes of $Ni_{52}Ti_{48-x}Co_x$ ($x = 0$, 1.5 and 4%) ternary SMAs in 0.9% NaCl solution at 37 °C using various electrochemical techniques, complemented with SEM/EDX and full XPS studies. The passivation impact of alloyed Co is translated into an obvious enhancement in the corrosion resistance of these materials.

2. Experimental

2.1. Materials

The working electrodes employed in this work were made of NiTiCo SMAs of chemical composition $Ni_{52}Ti_{48-x}Co_x$ ($x = 0$, 1.5, and 4.0 Co at%). These alloys were fabricated by melting Ni, Ti and Co elements of purity higher than 99.99% in induction vacuum furnace, as fully described elsewhere.[34] Rods of these alloys were used for electrochemical measurements. Such rods were mounted in a polyester resin leaving an exposed area of $\sim$0.2 cm^2. Before each run, the working electrodes were wet ground using a silicon carbide paper (600-grit), washed in distilled water, and finally rinsed with absolute ethanol.

2.2. Electrochemical setup and solutions

Electrochemical measurements were performed in a standard jacketed three-electrode cell, with a saturated calomel electrode (SCE) and a Pt mesh electrode serving respectively as reference electrode and auxiliary electrode. This standard electrochemical cell was linked to a PC-connected potentiostat/galvanostat AUTOLAB (PGSTAT30) to run and record the various electrochemical techniques employed in this work. Measurements were conducted in a normal saline solution, namely 0.9% NaCl, freshly prepared using water purified by a Millipore Milli-Q system (18.2 MΩ cm). The used salt was analytical grade purchased from Sigma-Aldrich. Solution temperature was maintained constant at (37 ± 0.2 °C) using a temperature-controlled water bath, FP40-MA Refrigerated/Heating Circulator, with its water being circulating through the outer cell jacket.

2.3. Electrochemical measurements

2.3.1. Uniform corrosion studies. The uniform corrosion behavior of the studied alloys was assessed using various electrochemical techniques, including DC polarization techniques (LPR and LSV) and dynamic impedance studies (DEIS). In all cases, the working electrode is first fully stabilized *via* recording its open-circuit-potential (E_{OC}) over 24 h. DEIS measurements were then performed at the respective

corrosion potential (E_{corr}), determined from the E_{OC} *vs.* time plots. The frequency range was set as 50 kHz to 0.05 Hz with 8 points per decade of frequency. AC perturbation amplitude was 15 mV. Measurements were performed once a day for a period of seven days in 0.9% NaCl at 37 °C. DEIS experiments were followed by LPR measurements, recorded by scanning the potential of the working electrode within a narrow range around E_{corr} ($E_{corr} \pm 20$ mV) at a scan rate of 1.0 mV s^{-1} starting from the negative potential. Electrochemical uniform corrosion studies were complemented by measurements in Tafel's polarization range, namely ($E = E_{corr} \pm 250$ mV).

2.3.2. Anodic behaviour (passivity and breakdown of passivity). The effect of Co addition on the anodic behaviour and passive layer growth kinetics and breakdown on the studied SMAs was also investigated employing LSV and chronoamperometry techniques. The former technique was carried out *via* scanning the potential of the working electrode linearly from a cathodic potential of −2.0 V (SCE) up to an anodic potential of +2.0 V (SCE) with a scan rate of 1.0 mV s^{-1}. For chronoamperometry technique, the working electrode was first held at −2.0 V (SCE) for 60 s to achieve a reproducible electrode surface, then anodically polarized with sweep rate of 1.0 mV s^{-1} up to a certain applied anodic potential, E_a. Finally, the working electrode was held at E_a, where the anodic current was monitored for 5 min.

The reproducibility was ensured *via* repeating each run at least three times. Arithmetic mean and standard deviation of the various electrochemical parameters were calculated and reported.

2.4. Surface characterizations

Prior to microscopic and spectroscopic investigations, the SMA samples undergone mechanical pretreatment by means of grinding (waterproof abrasive papers SiC 240, 600, 1200 and 2500) and polished (diamond suspension 6 and 1 μm, with a finish on 0.05 μm silica). Both of these processes were carried out using Digiprep 251 (Metkon, Turkey).

Microstructural analysis was carried out using scanning electron microscopy (SEM), S-3400N (Hitachi, Japan) with a tungsten electron source. Back-scatter electron (BSE) mode was utilized, operating at an accelerating voltage of 20 kV, for better contrast of metallic phases. The SEM images of polished surface of various investigated SMA alloys were analyzed using the program for data visualization and analysis (Gwyddion, 2.40, Czech Republic).[35]

X-ray photoelectron spectroscopy (XPS) was used for the evaluation of the long term exposure effect of the as-prepared $Ni_{52}Ti_{48-x}Co_x$ alloys ($x = 0$, 1.5 and 4.0%). The measurements were performed for as-polished sample and after 7 days immersion in 0.9% NaCl solution at 37 °C. After this treatment, the samples were cleaned in deionized water (2× 10 min) and dried. No other treatment was implemented in order not to compromise the subtle chemical changes on the surface. Analysis was performed for titanium, nickel, cobalt, chlorine and oxygen.

3. Results and discussion

3.1. Uniform corrosion studies

3.1.1. Monitoring open-circuit potential (E_{OC}). Monitoring E_{OC} of a given alloy/solution interface is important in defining its domains of corrosion (passivation/depassivation) and achieving a steady-state potential value, E_{ss}.[36] Fig. 1 shows the effect of Co addition on the E_{OC} *vs.* time (up to 24 h) characteristics of the tested SMA, namely $Ni_{52}Ti_{48}$ (designated here as Alloy I). Different amounts (1.5 and 4%) of alloyed Co were added to Alloy I at the expense of Ti, yielding two ternary SMAs with increased amounts of alloyed Co, namely $Ni_{52}Ti_{46.5}Co_{1.5}$ (Alloy II), and $Ni_{52}Ti_{44}Co_4$ (Alloy III). Measurements were conducted in 0.9% NaCl solution at 37 °C.

For all tested alloys, within the first moments of immersion, E_{OC} shifts towards nobler values, denoting passivation. This passivation behavior is most probably due to the high reactivity of the alloying elements (Ni, Ti, and Co), which induced an initial formation and growth of a passive oxide film. After its initial rise, E_{OC} decays, referring to depassivation (oxide thinning/dissolution) induced by Cl^- anions in solution, to a reasonably steady value (E_{ss}). This behaviour indicates the occurrence of two opposite processes (passivation and destabilization of the passive layer) competing each other. The former, when predominates, impedes Cl^- adsorption and oxide dissolution is subsequently delayed, drifting E_{OC} to nobler values. The later process (passivity destabilization as a result of the aggressive attack of Cl^- anions) activates the alloy surface thus, dragging E_{OC} back toward active values. The competition between these two counter-acting processes may explain the appearance of potential fluctuations and a hump in the $E_{OC} - t$ curves of Alloy I and Alloy II, respectively. The ennoblement of both the hump's height and E_{ss} upon the addition of alloyed Co may refer to improved passivation. These findings demonstrate, under these experimental conditions, that the addition of 1.5% alloyed Co to Alloy I can improve its corrosion resistance, but not enough to ensure efficient passivation. Further increase in the Co content (up to 4 at% in this study, Alloy III) has resulted

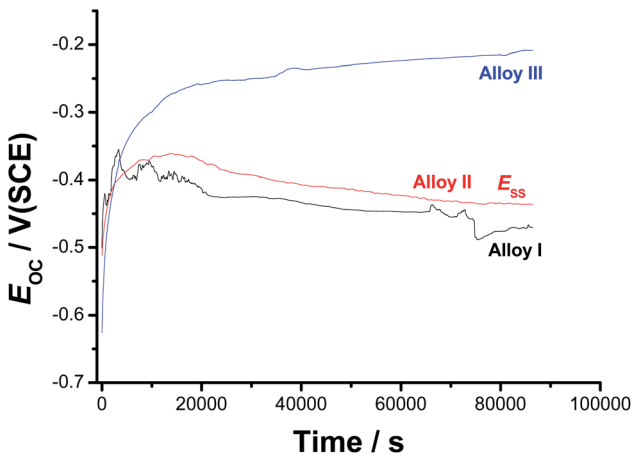

Fig. 1 Open-circuit potential (E_{OC}) *vs.* time (up to 24 h) responses of the three tested SMAs recorded in 0.9% NaCl solutions at 37 °C.

in an efficient passivation during the period of that operation (24 h); the passivation of Alloy III continues till the end of the operation, where E_{ss} is attained.

In spite of its tendency to passivate in these solutions, passivity of the Co-free SMA (*i.e.*, Alloy I) turns to be weak and unstable compared with that of Alloy II and Alloy III, as indicated by current oscillations and the obvious decay in E_{OC} till E_{ss}. Its E_{ss} value is always more negative than those measured for Alloys II and III. This means that the surface of Alloy I is more susceptible to corrosion in 0.9% NaCl than the surfaces of Alloys II and III. These results highlight the influence of the alloyed Co on the sample passivation.

After 7 days of free corrosion in 0.9% NaCl solution at 37 °C, optical microscopy examination (Fig. 2) revealed that, in all cases, the corrosion pits (formed as a result of the aggressive attack of Cl^- anions) are surrounded on all sides by regions covered with a protective oxide layer (passivity). Obviously, in presence of the alloyed Co, areas of passivity significantly increase at the expense of those of pits. This means that the pit area density (*i.e.*, the ratio of pit area to total surface area) diminishes with alloyed Co content, suggesting better passivation impact of the alloyed Co and subsequent increase in the corrosion resistance.

3.1.2. Polarization measurements. Monitoring E_{OC} study (Fig. 1) revealed an obvious progressive positive shift in E_{OC} with increasing the percentage of alloyed Co. This suggests anodic reaction kinetics controlled by the alloyed Co, and the extent of this reaction kinetic control depends on Co content. To confirm this result, cathodic and anodic polarization curves were recorded for each alloy, as shown in Fig. 3. Polarization measurements were conducted in 0.9% NaCl at a scan rate of 1.0 mV s^{-1} at 37 °C. From Fig. 3, there is an obvious increase in the cathodic and anodic overpotentials, with anodic overpotentials being much more affected than the cathodic ones, with increase in the amount of alloyed Co in the studied alloys. Extrapolation of polarization curves allows for determination of

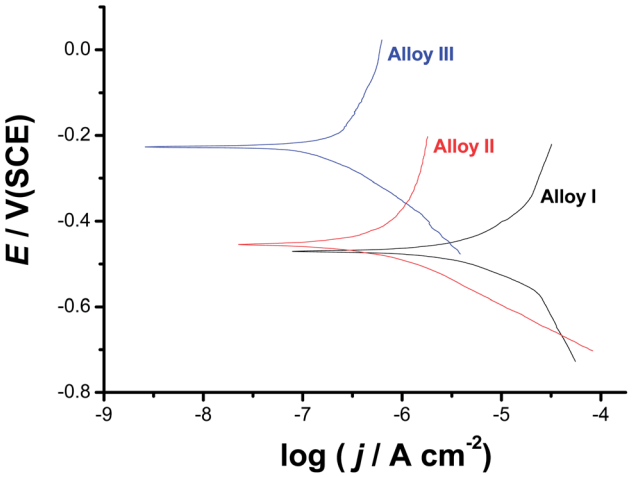

Fig. 3 Cathodic and anodic polarization curves recorded for the three tested SMAs in 0.9% NaCl solution at a scan rate of 1.0 mV s^{-1} at 37 °C.

corrosion potential (E_{corr}) as well as corrosion current density (j_{corr}), and eventually investigated metal uniform corrosion rate through Faraday's law.[37]

The obvious decrease in j_{corr} with increase in Co content is a strong evidence for the influence of alloyed Co on the surface passivation. This is clear from Table 1, where Alloy III (the SMA with the highest content of alloyed Co, 4.0 at%) recorded the least j_{corr} value (0.26 μA cm^{-2}) among the other tested alloys (j_{corr}: 14.1 and 0.62 μA cm^{-2} for Alloy I and Alloy II, respectively). In addition, the corrosion potential (E_{corr}) drifts towards nobler values with increase in Co content, confirming passivation induced by alloyed Co. In order to gain more insight on the passivation influence of alloyed Co, polarization curves shown in Fig. 3 were analyzed using Tafel extrapolation method (ESI, Fig. S1†). The obtained data are listed in Table 1. A clear curvature, due to passivation induced by the alloyed Co, can be seen over the complete applied potential range of the anodic polarization curves, making calculation of the anodic Tafel

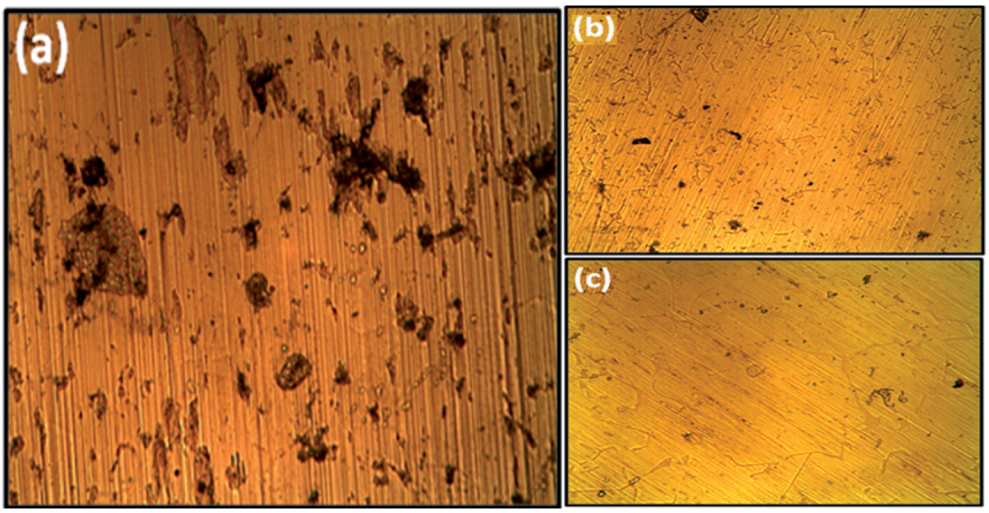

Fig. 2 Optical images (×2000) captured for the investigated $Ni_{52}Ti_{48-x}Co_x$ SMAs after 7 days of free corrosion in 0.9% NaCl solution at 37 °C: (a) x = 0.0% Co, (b) x = 1.5% Co, (c) 4.0% Co.

Table 1 Average (standard deviation) values of the various electrochemical kinetic parameters associated with polarization measurements for the three tested SMAs. Polarization measurements were conducted in 0.9% NaCl solution at a scan rate of 1.0 mV s^{-1} at 37 °C

	Tafel extrapolation		LPR	
Tested alloy	E_{corr}/mV(SCE)	j_{corr}/μA cm^{-2}	R_p/Ω cm^2	j_{corr}/μA cm^{-2}
Alloy I (0.0% Co)	−470(6)	14.1(0.2)	8954.2(35)	13.4(0.2)
Alloy II (1.5% Co)	−455(4)	0.62(0.1)	52 129.2(125)	0.75(0.14)
Alloy III (4.0% Co)	−227(3)	0.26(0.05)	203325(227)	0.33(0.08)

slopes inaccurate.[38–42] Therefore, McCafferty approach was applied here in order to estimate the anodic Tafel line under passivation conditions, see ESI† file for details (Section I).[37] The high values recorded for β_a (380–716 mV dec^{-1}), which refer to delay in the rate of alloy dissolution due to passivation, may also be considered as another evidence for the influence of the alloyed Co on the surface passivation.

Linear polarization resistance (LPR) measurements were also performed to gain more insight on the influence of alloyed Co on the uniform corrosion behavior of the tested SMAs. Such measurements were carried out in 0.9% NaCl solution at 37 °C. The potential was scanned around E_{corr} ($E = E_{corr} \pm 20$ mV) at a scan rate of 0.2 mV s^{-1} (Fig. 4). Polarization resistance ($R_p = (dE/dj)_{E=E_{corr}}$) values derived from the slopes of the LPR plots were inserted in the Stern–Geary equation[43] for accurate evaluation of j_{corr}.

$$j_{corr} = B/R_p = \{\beta_a\beta_c/2.303\ (\beta_a + \beta_c)\}/R_p \quad (1)$$

As can be seen, there is a good agreement between j_{corr} values obtained from the two polarization methods, namely Tafel extrapolation and LPR (Table 1). Thus, LPR method confirms the validity of Tafel extrapolation method in evaluating the uniform corrosion rates (expressed here as j_{corr} values).[44] Here again, Alloy III recorded the highest R_p value (203 325 Ω cm^2), and hence exhibits the highest corrosion resistance, among the tested alloys. This R_p value of Alloy III is 34 and 7 times greater than those measured for Alloy I (8954 Ω cm^2), and Alloy II (52 129 Ω cm^2), respectively.

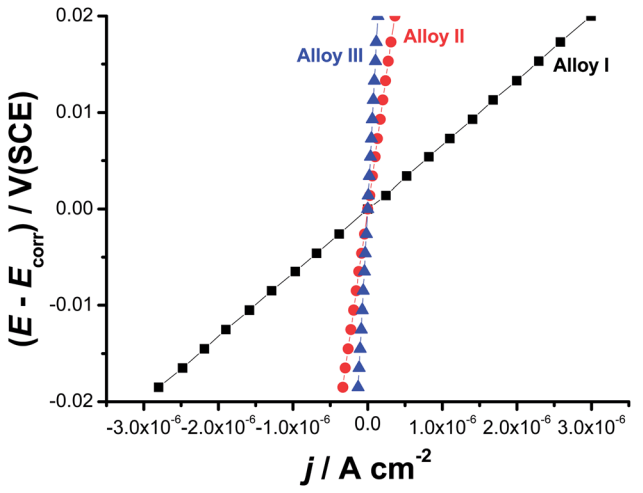

Fig. 4 Linear polarization resistance plots measured for the three tested SMAs in 0.9% NaCl solution at a scan rate of 0.2 mV s^{-1} at 37 °C.

3.1.3. Dynamic electrochemical impedance spectroscopy measurements (DEIS). Fig. 5 depicts the changes of DEIS impedance graphs in Nyquist projection upon samples' exposure to NaCl solution. The corresponding Bode plots are shown in Fig. S2 (ESI†). Each studied alloy owes similar size of spectra, yet the development of spectra differs between samples over time. Singular disturbances in spectra size are most likely the consequence of the pitting corrosion and pits re-passivation. The shape of the impedance spectra is representative of passive films forming on titanium alloys.[45] At this stage, the following conclusion could be drawn: low alloying component of cobalt decreases the corrosion resistance of investigated alloy. The behavior being apparent from the earliest moment and becomes more profound over time.

To fully address the changes of electric parameters of investigated samples and in particular the behavior of the passive layer, data should be analyzed with electric equivalent circuit (EEC). The structure of TiO_2 passive layer is composed of the inner, barrier layer and outer, porous layer of low resistivity.[44,45] For this reason, two time-constant electric equivalent circuits (EEC) are often used for fitting of impedance data.[46,47] However, due to the porous nature of the outer layer both of the time constants overlap on the impedance spectra, revealing capacitance dispersion. In these cases, the constant phase element (CPE) is often used, as it is capable to appropriately express normal time constant distribution from both the outer and the inner layer. CPE takes into account dispersion of capacitance behaviour, which originates from multiple factors, such as multiple layers, adsorption and diffusion processes, surface geometry and presence of intermetallic phases.[48–50] This type of model simplification is often used during impedance monitoring in order to obtain continuous trend of changes over time of exposure, which is required for proper representation of investigated system.[51–53] The effective capacitance can be further estimated on the base of CPE using estimation proposed by Hirschorn *et al.*[54,55]

While authors tested numerous EEC's, the best trend of changes together with the best fit (measured as Chi^2 parameter) was observed for R(QR) circuit (ESI, Fig. S3(d)†). Following equivalent circuit is commonly found to describe NiTi alloys exposed to electrolyte containing chloride ions.[56–60] R_{sol} stands for electrolyte resistance and R_{ct} for charge transfer resistance through metal/electrolyte interface. Constant phase element

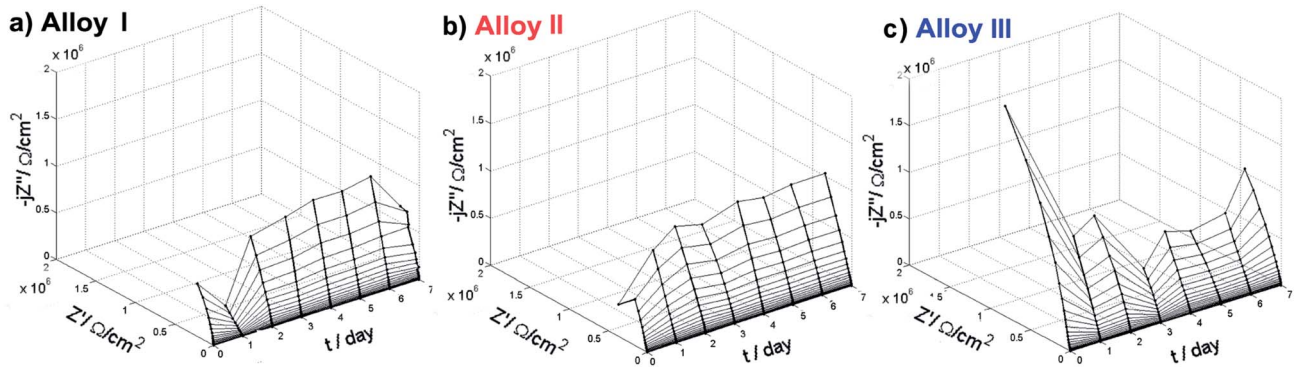

Fig. 5 Nyquist impedance plots *vs.* exposure time for each investigated SMA alloy in 0.9% NaCl under 37 °C.

(CPE) represents the capacitance of both the inner and the outer passive layer, while the smallest capacitance dominates CPE value. Admittance of CPE is given by equation $1/Z = Q_{CPE}(j\omega)^n$. It is worth noting that for $n = 1$, CPE describes a capacitor. The key contributing component is the breakdown of passive layer and initiation of pitting corrosion, leading to surface heterogeneities of the electrode properties. In the case of NiTi alloys, the passive layer consists mainly of titanium oxides, which has been confirmed by XPS analysis (see later).

Fig. S3(a), ESI,† displays the changes of quasi-capacitance Q with time of exposure in NaCl solution. The behavior is similar for each investigated alloy. Initially Q decreases and after 2–3 days it remains constant throughout the rest of experiment. Since the capacitance value is in reverse proportion to layer thickness, results prove the formation and stabilization of the passive layer. Fig. S3(c), ESI,† exhibits the charge transfer resistance changes during the experiment. It is important to state that each investigated alloy was characterized by very high value of this parameter, ranging from 0.5 up to even 10 MΩ cm^2. The highest increase of R_{ct} was observed for Alloy III, typically occurring after day 3. This effect corroborates with TiO_2 passive layer formation and testifies increase of corrosion resistance of investigated alloys.[61] On the other hand, gradual decrease of R_{ct} for Alloy I might correspond to deterioration of its protective properties and presence of pitting corrosion, as confirmed by other studies (SEM and XPS). Similar behavior was observed for other metals under pitting corrosion conditions.[61,62]

3.2. Anodic behavior (kinetics of passive layer growth and its breakdown)

Fig. 6 exhibits the potentiodynamic anodic polarization curves recorded for the studied alloys in 0.9% NaCl solution at a scan rate of 1.0 mV s^{-1} at 37 °C. Obviously, there is no active dissolution near the corrosion potential (E_{corr}), as the studied alloys tend to passivate in such solutions (revisit Fig. 1). Passivity of these materials was also evidenced from XPS analysis (see later). Passivity of Alloys II and III persists over a wide range of potential. It extends with a very low passive current (j_{pass}) up to the pitting potential, E_{pit}. Alloy I's passivity seems much weaker than that of Alloys II and III, as its j_{pass} is higher and enhances with potential (clearly seen the inset of Fig. 6). Once E_{pit} is reached, remarkable changes in the passive region have occurred. The passive current increased steadily with no sign for oxygen evolution, denoting passivity breakdown and initiation of pitting attack caused by Cl^- anions. Once initiated, pits are stabilized by the delocalized development of severe conditions originated from metal cation hydrolysis and migration of the aggressive Cl^- anions.[63]

The lower j_{pass} values of Alloys II and III, in addition to the remarkable positive (noble) shift in their E_{pit} values which resulted in an obvious increase in the pitting corrosion resistance R_{pit}, $R_{pit} = |E_{corr} - E_{pit}|$[63] as compared with Alloy I, confirm uniform corrosion studies (revisit Section 3.1), and adds another evidence for the passivation influence of alloyed Co.

Chronoamperometry (current (j)/time (t) transients) measurements were also recorded to gain more insight on the effect of Co addition on the kinetics of passive layer growth and passivity breakdown (Fig. 7). Measurements were recorded in 0.9% NaCl solutions at 37 °C at two applied anodic potentials, E_a, namely 0.5 and 1.5 V *vs.* SCE. The location of the former E_a value, namely 0.5 V *vs.* SCE is far below the E_{pit} value of any of the studied alloys, while that of the later (1.5 V *vs.* SCE) is

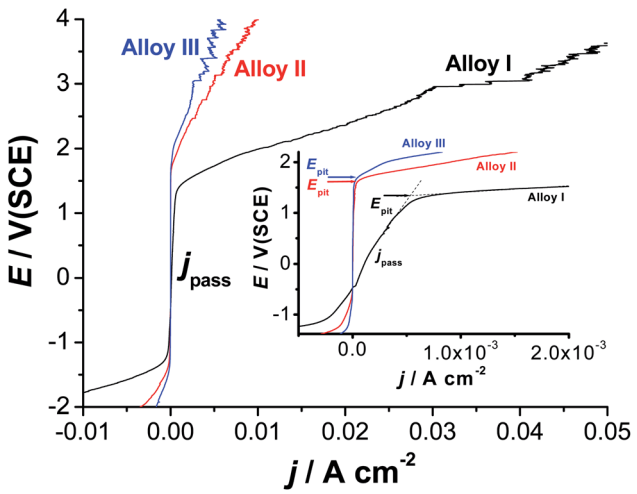

Fig. 6 Linear polarization curves recorded for the three tested SMAs in 0.9% NaCl solution at a scan rate of 1.0 mV s^{-1} at 37 °C.

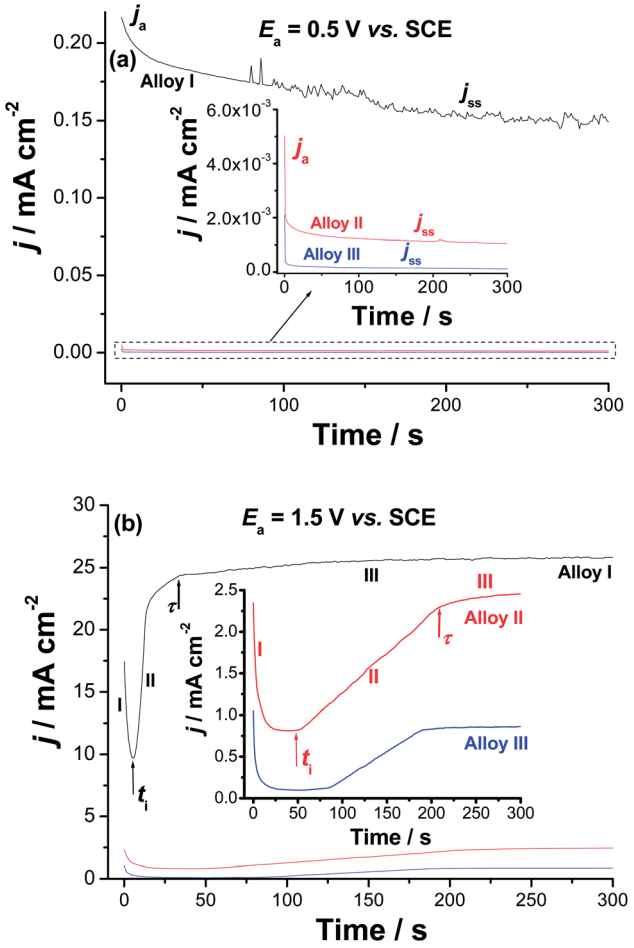

Fig. 7 Chronoamperometry (current *vs.* time) measurements recorded for the studied alloys in 0.9% NaCl solution at 37 °C at (a) $E_a = 0.5$ V *vs.* SCE and (b) $E_a = 1.5$ V *vs.* SCE.

beyond $(E_{pit})_{Alloy\ I}$ (1.25 V *vs.* SCE) and very close to $(E_{pit})_{Alloy\ II}$ (1.65 V *vs.* SCE) and $(E_{pit})_{Alloy\ III}$ (1.75 V *vs.* SCE), clearly seen in the inset of Fig. 6. The features vary according to the location of E_a with respect to E_{pit} and the chemical composition of the studied alloy.

When E_a is far from E_{pit} (Fig. 7a), for all samples, the j/t curves exhibit two stages for the passive layer growth. The anodic current (j_a) decreases with time during the first stage, denoting passive layer formation and growth. This decay in current is followed by a steady-state, the current passing through the passive film, j_{ss} (or j_{pass}), referring to a passive film of constant thickness. This constancy of the passive film thickness is most probably due to a balance between the rates of the passive layer growth and dissolution. The balance between such two counter-acting processes makes the oxide film hardly grows.[63–65]

On the other hand, as E_a approaches E_{pit}, the three studied alloys exhibit j–t curves with three distinct stages (Fig. 7b). The first stage is the passivation stage, as its current falls with time. The second stage involves passivity breakdown and subsequent pit formation and growth. Stage II started when the current of the first stage reached its minimum value. This has occurred at a certain time called the incubation time (t_i); the time the aggressive Cl^- anions need to remove the passive film locally and reach the base metal.[66–70] The current associated with this stage is termed as the pit growth current, j_{pit}. Stage II ends at another time (τ), denoting the onset of the last steady-state stage (stage III), during which the products of the pitting corrosion process are expected to precipitate inside the pits thus, hindering current flow through such blocked pits. In the same time, the current tends to grow as a result of metal dissolution due to pitting. Steady-state of the last stage is attained when the current rise due to metal dissolution (pit formation) is balanced by current decay caused by pitting corrosion products' blockade of the formed pits.

It follows from Fig. 7 that the rate of j_a decay (*i.e.*, rate of passivation) of Alloys II and III (see the inset of Fig. 7a) is much higher than that of Alloy I. In addition, j_{ss} diminishes significantly from Alloy I to Alloys II and III. The lower passivation rate and higher j_{ss} values of Alloy I, together with the obvious oscillations in its j_{ss} (see Fig. 7a) are strong evidences for its weak passivity compared with Alloys II and III. The weak passivity of Alloy I compared to Alloys II and III is also evident from Fig. 7b. This is clear from its shorter t_i and higher j_{pit} values (*i.e.*, higher susceptibility toward pitting corrosion) as compared with those measured for Alloys II and III. Thus, Alloys II and III tend to passivate in these solutions much more effectively than Alloy I. These results provide another proof for the passivation impact of alloyed Co, which strengthens alloy's passivity making it more resistant to passivity breakdown and subsequent pitting attack.

3.3. Role of alloyed Co

3.3.1. Microstructure studies. The microstructure of the investigated NiTiCo alloys with various Co content is shown in Fig. 8. It consists of austenite phase as a parent phase and martensite phase as a matrix phase in addition to precipitation of intermetallic compound of Ti_2Ni phase. The phase volume fraction (V_f) found in the microstructure is influenced by the Co addition. The V_f of austenite phase, parent phase, decreases by increasing Co content from 0 to 1.5 at% and almost vanishes from the microstructure when the Co content reached 4 at%. In the same time, V_f of the martensite phase increases with increasing the Co content, and the microstructure became fully martensitic when Co content increased to 4 at%, Fig. 8(c). Moreover, Co addition decreased the density of the Ti_2Ni phase in the microstructure of TiNi shape memory alloys.[71] The precipitates of Ti_2Ni phase and the spectrum of its chemical composition in the microstructure of NiTiCo (0 at% Co) are displayed in Fig. S4, ESI.† Ti content in Ti_2Ni phase is 65.85 at%, while Ni concentration is 34.15 at%.[65,66] Moreover, Co content in Ti_2Ni phase increased with increasing Co content in NiTi alloys. Additionally, the chemical composition of the matrix phase, martensite, in the TiNi (0 at% Co) SMA contains ≈52 at% Ni and 48 at% Ti. These percentages of Ni, Ti and Co in the martensite phase are found to vary according to %Co added to the TiNi SMA. For instance, Ni content is found to decrease in the martensite phase as %Co added to the alloy increases.

To further assess the effect of alloyed Co on the microstructure of the NiTi SMA, the samples were polished and

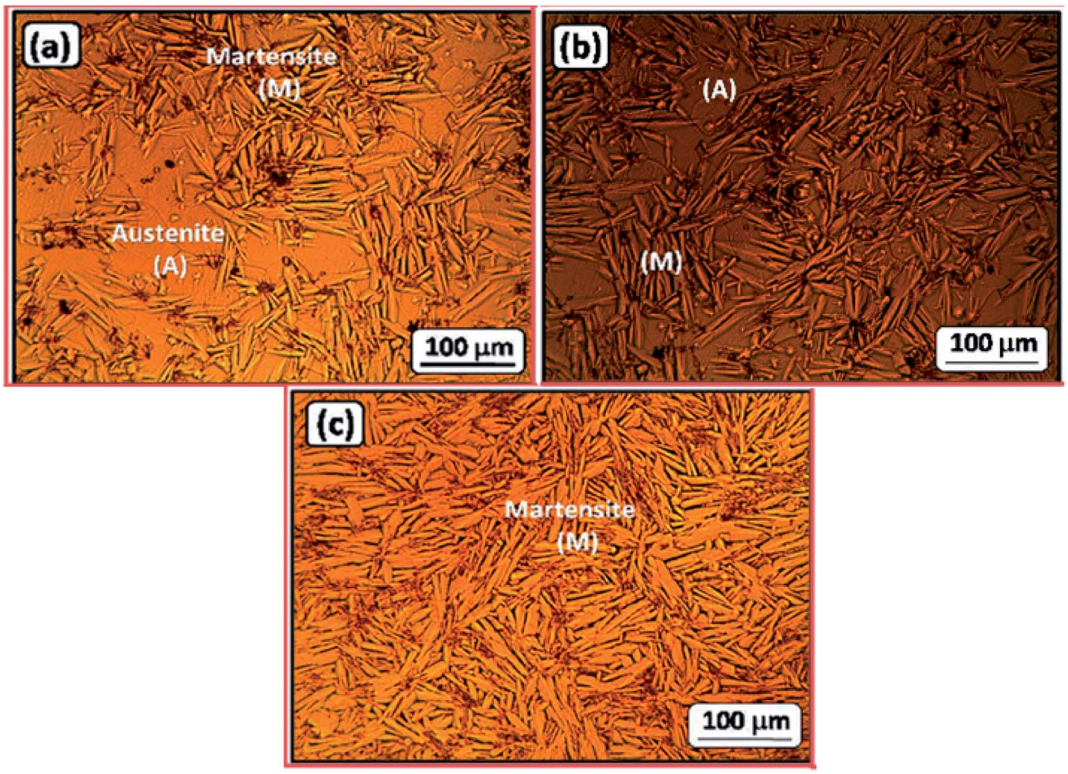

Fig. 8 SEM microstructure analysis of NiTiCo alloys: (a) 0.0% Co, (b) 1.5% Co, and (c) 4.0% Co.

imaged by SEM (Fig. S5, ESI†). These images have further undergone processing using Gwyddion software for evaluation of the average grain size and coverage of the Ti_2Ni phase, here colored red. The results of these analyses (ESI, Fig. S6†) revealed that the grain size of Ti_2Ni particles and V_f decrease with increasing Co content. These findings are in accordance with the previous results reported by El-Bagoury.[71–73] Furthermore, the TiNi–1.5%Co sample (Alloy II) shows an unexpected pattern of intermetallic phase (supposedly Ti_2Ni), that is longitudinal, thin and often appears to be curled. More insight into the microstructure of this sample is discussed in Fig. S7 (ESI†).

The multi-phase microstructure of the studied alloys helps to form micro-galvanic cells, and hence favors corrosion. Such galvanic cells are expected to form between Ti_2Ni precipitates, which function as anodes, and the other phases serving as cathodes. The variation in the chemical composition among the different phases in the microstructure may explain the obvious variation of the rates of corrosion of the studied SMAs. The presence of Co as an alloying element in such alloys decreased, as evidenced from the above electrochemical measurements, their rates of corrosion proportionally to its amount included in the alloy's matrix.

The obvious increase in the percentage of surface covered by the matrix (the passive region), (ESI, Fig. S8†), at the expense of the average grain area of the Ti_2Ni intermetallic phase (anodic regions, the corroded areas), with Co content may account for the improved corrosion resistance of the Co-containing NiTi alloys (Alloys II and III). Another important reason behind the increased corrosion resistance of these alloys with increasing the Co content is the passivation influence of the alloyed Co. XPS examinations were performed to confirm the passivation impact of alloyed Co, *vide infra*.

3.3.2. XPS analysis. X-ray photoelectron spectroscopy (XPS) has been utilized to evaluate the effect of long term exposure of as-prepared $Ni_{52}Ti_{48-x}Co_x$ (x = 0, 1.5 and 4.0 at%) alloys. The measurements were performed for as-polished sample and after 7 days immersion in 0.9% NaCl solution at 37 °C. After exposure, the samples were cleaned in deionized water (2× 10 min) and dried. No other treatment was implemented to limit the subtle chemical changes on the surface. Fig. 9a and b show high-resolution spectra changes as a result of exposition for both most notable alloy components Ti and Ni, respectively. Full chemical composition is depicted in Table 2. The most dominant component in Ti_{2p} spectrum, prior to exposition, was recorded at energy range of 454.2 eV and is ascribed to metallic titanium, while other peaks found at the surface are attributed to TiO_2 and Ti_2O_3 oxides, with $Ti_{2p3/2}$ peak located at BE of 458.6 and 455.5 eV, respectively. On the other hand, $Ni_{2p3/2}$ was deconvoluted using two peak doublets ascribed to metallic Ni at 852.7 and $Ni(OH)_2$ at 856.0 eV. Similar deconvolution was applied for cobalt, as presented on Fig. 9d. Co_{2p} spectrum revealed the presence of two components, attributed to the metallic cobalt and Co_3O_4 at BE of 777.9 and 779.9 eV, respectively. The position of these peaks is in good agreement with literature data.[31,74–78] Full chemical analysis was summarized in Table 3. High-resolution O_{1s} spectra were also recorded. The shape of these spectra suggested the presence of three pronounced components. The main component is located at

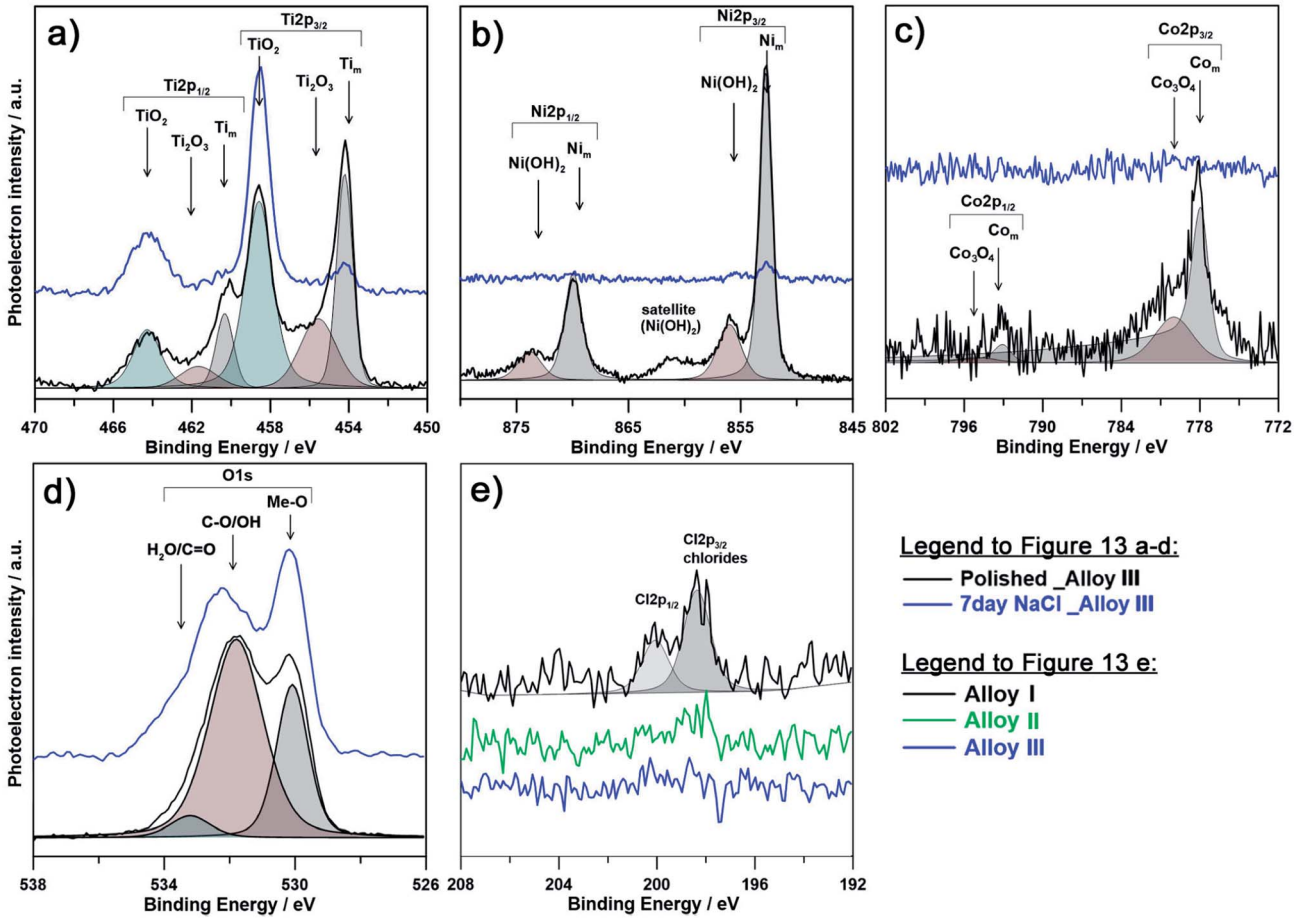

Fig. 9 High-resolution XPS spectra recorded in the binding energy region of (a) Ti_{2p}, (b) Ni_{2p}, (c) Co_{2p3} and (d) O_{1s} for as-polished Alloy III ($Ni_{52}Ti_{44}Co_4$) samples before and after 7 days immersion in 0.9% NaCl at 37 °C; (e) spectra recorded for Cl_{2p} region for each investigated alloy after the exposure.

~532.1 eV and often ascribed to hydroxyl groups on metal surface.[79–81] The second component, BE at 529.8 eV, is due to the metal oxide species and typically separated by 1.5–2.0 eV *versus* hydroxyl group component. Finally, the last peak at 533.1 eV is often ascribed to chemisorbed water, in particular in the outer porous passive layer.[81,82] It must also be noted that carbon-oxygen compounds, a common contaminant resulting from exposure to atmospheric air, influence the intensity of the first and third peak, as denounced on Fig. 9d. For this reason, O_{1s} contribution was not considered within analysis presented in Table 3. The total share of C_{1s} and O_{1s} as a contamination did not exceed 20%.

The chemical composition of the passive layer was similar for each investigated alloy prior to immersion in 0.9% NaCl aqueous solution. The presence of metallic component for each alloying element suggests low film thickness, not exceeding 12 nm, taking into consideration depth of XPS analysis. Both Ti and Ni spectra differ significantly as a result of immersion in

Table 2 Chemical composition, determined by XPS analysis, of investigated alloys for as-polished samples and as a result of 7 days immersion in 0.9% NaCl solution

	Ti_m	TiO_2	Ti_2O_3	Ni_m	$Ni(OH)_2$	Co_m	Co_3O_4	Cl	O
BE [eV]	454.2	458.6	455.5	852.7	856.0	777.9	779.9	198.3	530.1
As-polished									
Alloy I	10.1	16.6	8.4	19.3	7.4	—	—	—	38.2
Alloy II	10.0	15.1	7.0	18.5	5.9	4.3	1.2	—	38.0
Alloy III	10.1	16.3	7.3	19.4	6.2	3.7	1.0	—	36.0
After exposure									
Alloy I	3.7	24.6	2.6	4.5	2.8	—	—	2.5	59.3
Alloy II	2.8	25.4	2.2	4.4	1.7	—	0.9	1.2	61.4
Alloy III	6.5	25.0	1.9	2.8	1.7	—	1.2	—	60.9

Table 3 Chemical composition of oxygen compounds, determined by XPS analysis in the O_{1s} energy range for each investigated alloy before and as a result of 7 days immersion in 0.9% NaCl solution

	O-Me	OH/CO	H_2O	Ratio	
BE/eV	529.8	531.1	533.1	$OH : O^{2-}$	$H_2O : OH$
As-polished					
Alloy I	13.2	67.3	19.5	5.1 : 1	0.29 : 1
Alloy II	18.3	72.4	9.3	4.0 : 1	0.13 : 1
Alloy III	19.8	69.8	10.4	3.5 : 1	0.15 : 1
After exposure					
Alloy I	51.5	39.3	9.2	0.8 : 1	0.23 : 1
Alloy II	49.0	40.8	10.2	0.8 : 1	0.25 : 1
Alloy III	36.1	53.5	10.4	1.5 : 1	0.19 : 1

NaCl solution. Primarily, the exposition influenced the passive state by formation of TiO_2, and to a lesser extent Ti_2O_3. A decrease of the amount of metallic Ti and Ni suggests an increased passivation layer thickness, while amount of Co_m is on the level of the spectrometer threshold. Due to exposure and growth of the passive layer the cobalt peaks are barely distinguishable, even for Alloy III containing the highest Co content. It is important to note, that the surface of the passivated samples is mostly composed of titanium oxides, since the free energy for its formation is almost four times higher than that for nickel oxides.[59] Similarly, the amount of cobalt is barely distinguishable suggesting its absence in the outer passive layer.

The explanation for better corrosion resistance of alloy with higher cobalt content (Alloy III) can be made based on the amount of detected chlorine in the form of chlorides. As can be seen on Fig. 9e and Table 3, the highest amount of chlorides (as high as 2.5 at%) was found for Alloy I (0% Co). These results corroborate with poor behavior of Alloy I under electrochemical examination and correspond well with theory of breakdown of the passive layer and initiation of pitting corrosion. On the other hand, the amount of chlorides for Alloy III (4% Co) was below the analysis threshold, proving much higher corrosion resistance. Furthermore, there is a significant pattern observable between contribution from Ti_m component and amount of alloyed Co. Alloy I has much lower Ti_m in analyzed spectra, which can be speculatively related to thicker, yet less compact passive layer. This conclusion corroborates with the information drawn on the base of changes in the chemistry of O_{1s} spectra. It was revealed that for each investigated alloy, the as-polished sample is composed primarily of oxygen bound in hydroxyl groups (and oxygen due to air contamination), while as a result of the exposure to the corrosive medium (0.9% NaCl solution), the OH : Me-O ratio drops significantly indicating passivation, primarily in the form of TiO_2. It should be noted that the chemistry of Alloy III is proved to be chemically stable and affected the least among investigated samples. At the same time, the passive film on the surface of Alloy III is to the smallest extent composed of chemisorbed water species, a feature characteristic for passive films possessing high corrosion resistance (see Table 3).[79–82]

3.4. SEM studies

The SEM images of SMA alloys after 7 days exposure in 0.9% NaCl at 37 °C are summarized in Fig. S9 (ESI†). These micrographs corroborate the results of both electrochemical and XPS studies about the positive influence of alloying cobalt on the corrosion resistance of SMAs. The lowest rate of failure has been recognized for Alloy III sample, where corrosion was only observed in the form of partial selective dissolution of anodic precipitates Ti_2Ni. For Alloys I and II, much larger damage was observed, revealing initiation of corrosion failure on microstructure. Both size and number of corrosion pits are increasing with decreasing the cobalt content. Initiation of pitting corrosion by such micro-galvanic cells is often found in literature.[56] Eventually, large pits of several hundred microns can be traced on the surface of Alloy I. The failure of material under exposure to chloride ions was further confirmed by XPS examination.

4. Conclusion

Cobalt addition influences the microstructure of the tested SMAs through lowering the average size of Ti_2Ni intermetallic phases as well as the overall area covered by these phases. It is highly possible, that one of the ways for cobalt to affect the corrosion resistance is through homogenization of surface electrochemical properties and decreased activity of micro-galvanic cells. The amount of chloride ions adsorbed onto the passive layer covering the investigated SMAs greatly diminishes with the addition of alloyed Co, thus proving the stability of the passive layer and explaining enhanced resistance to uniform and pitting corrosion processes. Nevertheless, the chemistry of passive layer does not dramatically change, being primarily composed of titanium oxide TiO_2. The very high corrosion resistance of the investigated alloys was confirmed by impedance studies, where the charge transfer resistance through Co-enriched Alloy III sample was the highest and even improved during the exposition to corrosive environment.

Conflicts of interest

There are no conflicts to declare.

Acknowledgements

The authors acknowledge the financial aid received from Taif University, Saudi Arabia (Project Number 5486-438-1).

References

1 L. Kovarik, F. Yang, A. Garg, D. Diercks, M. Kaufman, R. D. Nobe and M. J. Mills, *Acta Mater.*, 2010, **58**, 4660–4673.
2 S. U. Rehman, M. Khan, A. Nusair Khan, L. Ali, S. Zaman, M. Waseem and S. H. I. Jaffery, *Mater. Sci. Eng., A*, 2014, **619**, 171–179.
3 S. H. Hong, J. T. Kim, H. J. Park, Y. S. Kim, J. Y. Suh, Y. S. Na, K. R. Lim, C. H. Shim, J. M. Park and K. B. Kim, *J. Alloys Compd.*, 2017, **692**, 77–85.

4 X. L. Meng, H. Li, W. Cai, S. J. Hao and L. S. Cui, *Scr. Mater.*, 2015, **103**, 30–33.
5 D. Jiang, C. M. Landis and S. Kyriakides, *Int. J. Solids Struct.*, 2016, **100–101**, 41–53.
6 C. Elibol and M. F. X. Wagner, *Mater. Sci. Eng., A*, 2015, **621**, 76–81.
7 A. N. Bucsek, G. A. Hudish, G. S. Bigelow, R. D. Noebe and A. P. Stebner, *Shape Memory and Superelasticity*, 2016, vol. 2, pp. 62–79.
8 O. Benafan, R. D. Noebe, S. A. Padulall, D. J. Gaydosh, B. A. Lerch, A. Garg, G. S. Bigelow, K. An and R. Vaidyanathan, *Scr. Mater.*, 2013, **68**, 571–574.
9 N. A. Zarkevich and D. D. Johnson, *Phys. Rev. Lett.*, 2014, **113**, 265701.
10 P. Chowdhury, L. Patriarca, G. Ren and H. Sehitoglu, *Int. J. Plast.*, 2016, **81**, 152–167.
11 C. Chluba, W. Ge, R. Lima de Miranda, J. Strobel, L. Kienle, E. Quandt and M. Wutting, *Science*, 2015, **348**, 1004–1007.
12 P. Chowdhury and H. Sehitoglu, *Fatigue Fract. Eng. Mater. Struct.*, 2016, **39**, 652–674.
13 P. Chowdhury, H. Sehitoglu and R. Rateick, *Curr. Opin. Solid State Mater. Sci.*, 2016, **20**, 140–150.
14 R. Basu, M. Eskandari, L. Upadhayay, M. A. Mohtadi-Bonab and J. A. Szpunar, *J. Alloys Compd.*, 2015, **645**, 213–222.
15 H. E. Karaca, E. Acar, G. S. Ded, S. M. Saghaian, B. Basaran, H. Tobe, M. Kok, H. J. Maier, R. D. Noebe and Y. I. Chumlyakov, *Mater. Sci. Eng., A*, 2015, **627**, 82–94.
16 M. Schmidt, J. Ullrich, A. Wieczorek, J. Frenzel, A. Schütze, G. Eggeler and S. Seelecke, *Shape Memory and Superelasticity*, 2015, **1**, 132–141.
17 I. Gotman, *J. Endourol.*, 1997, **11**, 383–389.
18 M. Navarro, A. Michiardi, O. Castano and J. A. Planell, *J. R. Soc., Interface*, 2008, **5**, 1137–1158.
19 T. Sawaguchi, T. Maruyama, H. Otsuka, A. Kushibe, Y. Inoue and K. Tsuzaki, *Mater. Trans.*, 2016, **57**, 283–293.
20 S. Alkan, P. Chowdhury, H. Sehitoglu, R. G. Rateick and H. J. Maier, *Int. J. Fatigue*, 2016, **84**, 28–39.
21 N. S. Manam, W. S. W. Harun, D. N. A. Shri, S. A. C. Ghani, T. Kurniawan, M. H. Ismail and M. H. I. Ibrahim, *J. Alloys Compd.*, 2017, **701**, 698–715.
22 J. M. Jani, M. Leary, A. Subic and M. A. Gibson, *Mater. Des.*, 2014, **56**, 1078–1113.
23 R. I. M. Asri, W. S. W. Harun, M. Samykano, N. A. C. Lah, S. A. C. Ghani, F. Tarlochan and M. R. Raza, *Mater. Sci. Eng., C*, 2017, **77**, 1261–1274.
24 J. Khalil-Allafi, B. Amin-Ahmadi and M. Zare, *Mater. Sci. Eng., C*, 2010, **30**, 1112–1117.
25 N. Figueira, T. M. Silva, M. J. Carmezim and J. C. S. Fernandes, *Electrochim. Acta*, 2009, **54**, 921–926.
26 X. Huang, D. W. Norwich and M. Ehrlinspiel, *J. Mater. Eng. Perform.*, 2014, **23**, 2630–2634.
27 A. Fasching, D. Norwich, T. Geiser and G. W. Paul, *J. Mater. Eng. Perform.*, 2011, **20**, 641–645.
28 R.-r. Jing and F.-s. Liu, *Chin. J. Aeronaut.*, 2007, **20**, 153–156.
29 H. Soni, N. Sannayellappa and R. M. Rangarasaiah, *J. Mater. Res.*, 2017, **32**, 3100–3108.
30 B. G. Pound, *Corros. Rev.*, 2014, **32**, 21–41.
31 M. A. Amin, N. El-Bagoury, M. H. H. Mahmoud, M. M. Hessien, S. S. Abd El-Rehim, J. Wysocka and J. Ryl, *RSC Adv.*, 2017, **7**, 3635–3649.
32 E. Kassab, L. Neelakantan, M. Frotscher, S. Swaminathan, B. Maaß, M. Rohwerder, J. Gomes and G. Eggeler, *Mater. Corros.*, 2014, **65**, 18–22.
33 A. Phukaoluan, A. Khantachawana, S. Dechkunakorn, N. Anuwongnukroh, P. Santiwong and J. Kajornchaiyakul, *Adv. Mater. Res.*, 2012, **378–379**, 650–654.
34 N. El-Bagoury, M. A. Amin and H. Shokry, *Int. J. Electrochem. Sci.*, 2013, **8**, 1246–1261.
35 D. Neĉas and P. Klapetek, *Cent. Eur. J. Phys.*, 2012, **10**, 181–188.
36 A. M. Shams El Din, R. A. Mohammed and H. H. Haggag, *Desalination*, 1997, **114**, 85–95.
37 E. McCafferty, *Corros. Sci.*, 2005, **47**, 3202–3215.
38 H. J. Flitt and D. P. Schweinsberg, *Corros. Sci.*, 2005, **47**, 2125–2156.
39 H. J. Flitt and D. P. Schweinsberg, *Corros. Sci.*, 2005, **47**, 3034–3052.
40 F. Mansfeld, *Corros. Sci.*, 2005, **47**, 3178–3186.
41 B. Rosborg, J. Pan and C. Leygraf, *Corros. Sci.*, 2005, **47**, 3267–3279.
42 M. A. Amin, K. F. Khaled and S. A. Fadl-Allah, *Corros. Sci.*, 2010, **52**, 140–151.
43 M. Stern and A. L. Geary, *J. Electrochem. Soc.*, 1957, **104**, 56–63.
44 M. A. Amin, K. F. Khaled and S. A. Fadl-Allah, *Corros. Sci.*, 2010, **52**, 140–151.
45 R. M. Souto, M. M. Laz and R. L. Reis, *Biomaterials*, 2003, **24**, 4213–4221.
46 B. Schneider Gugelmin, L. Sopchenski Santos, H. de Araújo Ponte and C. E. Bruno Marino, *Mater. Res.*, 2015, **18**, 602–607.
47 M. A. Amin, H. Shokry and E. M. Mabrouk, *Corrosion*, 2012, **68**, 699–712.
48 A. Norlin, J. Pan and C. Leygraf, *J. Electrochem. Soc.*, 2006, **153**, B225–B230.
49 B. Sapoval, J. N. Chazalviel and J. Peyrière, *Phys. Rev. A*, 1988, **38**, 5867–5887.
50 T. Hu, Y. C. Xin, S. L. Wu, C. L. Chu, J. Lu, L. Guan, H. M. Chen, T. F. Hung, K. W. K. Yeung and P. K. Chu, *Mater. Chem. Phys.*, 2011, **126**, 102–107.
51 J. Ryl, L. Gawel, M. Cieslik, H. Gerengi, G. Lentka and P. Slepski, *Int. J. Electrochem. Sci.*, 2017, **12**, 6908–6919.
52 J. Ryl, J. Wysocka, M. Jarzynka, A. Zielinski, J. Orlikowski and K. Darowicki, *Corros. Sci.*, 2014, **87**, 150–155.
53 J. N. van der Meer, A. Pampel, E. J. W. Van Someren, J. R. Ramautar, Y. D. van der Werf, G. Gomez-Herrero, J. Lepsien, L. Hellrung, H. Hinrichs, H. E. Möller and M. Walter, *NeuroImage*, 2016, **125**, 880–894.
54 B. Hirschorn, M. E. Orazem, B. Tribollet, V. Vivier, I. Frateur and M. Musiani, *J. Electrochem. Soc.*, 2010, **157**, C458–C463.
55 B. Hirschorn, M. E. Orazem, B. Tribollet, V. Vivier, I. Frateur and M. Musiani, *Electrochim. Acta*, 2010, **55**, 6218–6227.
56 C. Liu, P. K. Chu, G. Lin and D. Yang, *Corros. Sci.*, 2007, **49**, 3783–3796.

57 X. L. Zhang, Z. H. Jiang, Z. P. Yao, Y. Song and Z. D. Wu, *Corros. Sci.*, 2009, **51**, 581–587.
58 M. M. Verdian, K. Raeissi and M. Salehi, *Corros. Sci.*, 2010, **52**, 1052–1059.
59 M. Chembath, J. N. Balaraju and M. Sujata, *Mater. Sci. Eng., C*, 2015, **56**, 417–425.
60 B. G. Pound, *J. Biomed. Mater. Res., Part A*, 2014, **102**, 1595–1604.
61 J. Orlikowski, J. Ryl, M. Jarzynka, S. Krakowiak and K. Darowicki, *Corrosion*, 2015, **71**, 828–838.
62 S. Krakowiak, K. Darowicki and P. Ślepski, *J. Electroanal. Chem.*, 2005, **575**, 33–38.
63 D. D. Macdonald, *J. Electrochem. Soc.*, 1992, **139**, 3434–3449.
64 M. A. Amin, S. S. Abd El-Rehim, F. D. A. Aarão Reis and I. S. Cole, *Ionics*, 2014, **20**, 127–136.
65 M. A. Amin, S. S. Abd El Rehim and A. S. El-Lithy, *Corros. Sci.*, 2010, **52**, 3099–3108.
66 S. Szklarska-Smialowska, *Pitting corrosion of metals, D. 296*, NACE, Houston, TX, 1986.
67 Z. A. Foroulis and M. J. Thubrikar, *J. Electrochem. Soc.*, 1975, **122**, 1296–1301.
68 R. T. Foley and T. H. Nguyen, *J. Electrochem. Soc.*, 1982, **129**, 464–467.
69 T. P. Hoar, *Corros. Sci.*, 1967, **7**, 341–355.
70 M. A. Amin, H. H. Hassan and S. S. Abd El Rehim, *Electrochim. Acta*, 2008, **53**, 2600–2609.
71 N. El-Bagoury, *Mater. High Temp.*, 2015, **32**, 390–398.
72 N. El-Bagoury, *Met. Mater. Int.*, 2016, **22**, 468–473.
73 N. El-Bagoury, *Mater. Sci. Technol.*, 2014, **30**, 1795–1800.
74 K. Siuzdak, M. Szkoda, J. Karczewski, J. Ryl and A. Lisowska-Oleksiak, *Electrochim. Acta*, 2016, **222**, 1281–1292.
75 K. Siuzdak, M. Szkoda, A. Lisowska-Oleksiak, J. Karczewski and J. Ryl, *RSC Adv.*, 2016, **6**, 33101–33110.
76 D. Briggs, in *XPS: basic principles, spectral features and qualitative analysis, in surface analysis by Auger and X-ray photoelectron spectroscopy*, ed. D. Briggs and J. T. Grant, IM Publications, Chichester, 2003, p. 31.
77 R. M. Wang, C. L. Chu, T. Hua, Y. S. Dong, C. Guo, X. B. Sheng, P. H. Lin, C. Y. Chung and P. K. Chu, *Appl. Surf. Sci.*, 2007, **253**, 8507–8512.
78 N. Ohtsu, K. Sakamoto, Y. Hirano and M. Yamane, *Surf. Interface Anal.*, 2016, **48**, 488–492.
79 J. Wysocka, S. Krakowiak and J. Ryl, *Electrochim. Acta*, 2017, **258**, 1463–1475.
80 M. A. Amin, M. Saracoglu, N. El-Bagoury, T. Sharshar, M. M. Ibrahim, J. Wysocka, S. Krakowiak and J. Ryl, *Int. J. Electrochem. Sci.*, 2016, **11**, 10029–10052.
81 E. McCaferty and J. P. Wightman, *Surf. Interface Anal.*, 1998, **26**, 549–564.
82 Q. Liu, X. Tong and G. Zhou, *Langmuir*, 2015, **31**, 13117–13126.